

# Modeling and simulation of multiple impacts of falling rigid bodies

Hua Shan<sup>a,\*</sup>, Jianzhong Su<sup>a</sup>, Florin Badiu<sup>a</sup>, Jiansen Zhu<sup>b</sup>, Leon Xu<sup>b</sup>

<sup>a</sup> *Department of Mathematics, University of Texas at Arlington, Arlington, TX 76019, United States*

<sup>b</sup> *Nokia Research Center, 6000 Connection Drive, Irving, TX 75039, United States*

Received 8 December 2004; received in revised form 8 June 2005; accepted 10 June 2005

---

## Abstract

When an electronic device drops at an inclination angle to the floor, the rapid successions of clattering sequence are important for their shock response to circuits, displays and disk drives. This article deals with both analytical and numerical analysis of multiple impacts. A three-dimensional computational dynamics code with a continuous contact impact model has been developed to simulate the multiple impacts of a falling rigid body with the ground. Results from the computational model as well as analytic analysis from a discrete contact impact model indicate that subsequent impacts might be larger than the initial impact in some situations. The differential equation based three-dimensional model is shown to be realistic in simulating a multiple-impact sequence and laid a foundation for detailed finite element analysis of the interior impact response of an electronic device.

© 2005 Elsevier Ltd. All rights reserved.

**Keywords:** Multiple impacts; Rigid body; Friction; Numerical simulation; Computational dynamics

---

## 1. Introduction

When an electronic device drops to the floor, it usually comes down with an inclination angle. After an initial impact at an uneven level, a rapid succession of clattering sequence occurs. There has been growing recognition that the entire impact sequence, rather than just the initial impacts are important for their shock response to circuits, displays and disk drives. In a pioneering study of Goyal et al. [1,2], it was found that when a two-dimensional rod was dropped at a small angle to the ground, the second impact might be as large as twice that of the initial impact. It therefore has raised the issue on how adequate the current testing procedure and simulation analysis are. Standard fragility tests that typically involve a single impact with no rotation, is not adequate for those types of drops. Angled dropping tests have been seen in the literature, but they are apparently more complicated in nature. Similarly, including subsequent impacts in numerical simulation will increase the computational costs. So there is a need for further study of multiple impacts from both analytical and numerical analysis as well as experiments.

The problems of single impact or the first impact are discussed in many articles in the mechanics and mathematical literature, see for example, [3–5] for rigid body collisions. Even in single-impact cases, the topic remains a focus of much discussion [6,7] as many theoretical issues of contact dynamics started to be resolved. Recent attention has been

---

\* Corresponding author. Tel.: +1 817 272 5685; fax: +1 817 272 5802.

E-mail address: [hshan@uta.edu](mailto:hshan@uta.edu) (H. Shan).

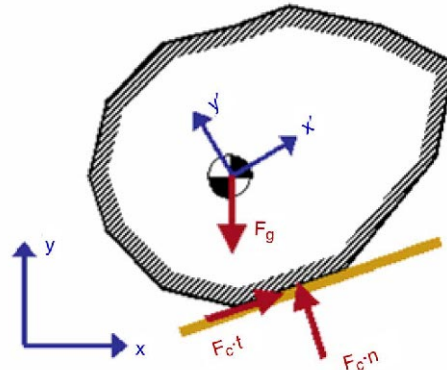


Fig. 1. Rigid body and coordinate systems.

paid to detect and calculate the micro-collisions that occur in a short time interval, when the bodies are flexible [8,9]. Various commercial software such as ANSYS etc. are available to study the single-impact problem; a rather detailed approach such as finite element analysis is also implemented [10,11].

The study of multiple impacts, however, is an emerging area. Goyal et al. [1,2] used a transition matrix method to calculate the clattering sequence and its impacts. There, the contact times of impacts are assumed to be instantaneous and the time intervals between the impacts are also brief, as a two-dimensional rod is dropped to the ground at a very small angle. We note here that these impacts are still relatively far apart in time, in comparison with the micro-collision situation [8]. These collisions occur at different parts of the body by following the motions of movement after the collisions, and are not a consequence of the elastic oscillations. Rather, the dynamics between the impacts plays a very significant role in determining the velocity and location of the next impact, particularly when the inclination angle at initial dropping is moderate.

In this study, we provide a comprehensive analysis of the clattering phenomena, and the work is therefore a continuation of the study by Goyal et al. [1,2]. Our results on the multiple impacts of a uniform rod are consistent with those of Goyal's. We further explore the scenario where a larger initial dropping angle leads to a different impact sequence. Our methodology and numerical tools allow us to consider the multiple-impact problem of a three-dimension non-uniform body with irregular geometry. Substantially new knowledge of the multiple impacts is gained with numerical experiments. Such research is a first step towards a simulation tool for the design and optimization of electronic components.

We outline our article as follows. In Section 2, we state the basic rigid body dynamics equation. Section 3 includes the continuous contact model that is used in numerical simulation. Section 4 contains theoretical clattering results of the two-dimensional uniform rod. We present the numerical simulation of the impacts of a three-dimensional rod in Section 5 and a three-dimensional simplified cell phone in Section 6. Discussion and conclusions are given in Section 7.

## 2. Rigid body dynamics model

Two sets of coordinate system are used to describe the displacement and rotation of the rigid body. The global coordinate system  $(x, y, z)$  is fixed to the ground, as shown in Fig. 1. The local coordinate system  $(x', y', z')$  or rigid body coordinate system is a body-fixed frame with its origin located at the mass center of the rigid body. In the present work, only the gravitational force  $\mathbf{F}_g$  and the impact contact force  $\mathbf{F}_c$  are considered.

The equation of unconstrained motion for the rigid body can be written as a set of ordinary differential equations in the following matrix form [12]:

$$\mathbf{M}\ddot{\mathbf{q}} = \mathbf{Q}_v + \mathbf{Q}_e \quad (1)$$

where  $\mathbf{q} = [\mathbf{R}^T, \boldsymbol{\beta}^T]^T$  is the vector of generalized coordinates,  $\mathbf{R} = \{x_c, y_c, z_c\}^T$  is the vector of the coordinate of the mass center, and  $\boldsymbol{\beta} = \{\beta_0, \beta_1, \beta_2, \beta_3\}^T$  is the vector of Euler parameters. The inertia matrix  $\mathbf{M}$  is given by

$$\mathbf{M} = \int_{\Omega} \rho \left[ -\mathbf{G}'^T \tilde{\mathbf{u}}'^T \mathbf{A}^T \right] [\mathbf{I}, -\mathbf{A} \tilde{\mathbf{u}}' \mathbf{G}'] d\Omega$$

where the integration is over the entire rigid body,  $\rho$  is the density,  $\mathbf{I}$  is the  $3 \times 3$  identity matrix,  $\mathbf{A}$  is the  $4 \times 4$  transformation matrix and  $\tilde{\mathbf{u}}'$  is the skew symmetric matrix obtained from the local coordinates vector  $\mathbf{u}'$ . The matrix  $\mathbf{G}'$  is a  $3 \times 4$  matrix expressed in terms of the Euler parameters as

$$\mathbf{G}' = 2 \begin{bmatrix} -\beta_1 & \beta_0 & \beta_3 & -\beta_2 \\ -\beta_2 & -\beta_3 & \beta_0 & \beta_1 \\ -\beta_3 & \beta_2 & -\beta_1 & \beta_0 \end{bmatrix}$$

$\mathbf{Q}_v$  the first term on the right-hand-side of Eq. (1) represents the vector that absorbs quadratic velocity terms.

$$\mathbf{Q}_v = - \int_{\Omega} \rho \left[ -\mathbf{G}'^T \tilde{\mathbf{u}}'^T \mathbf{A}^T \right] \boldsymbol{\alpha}_v d\Omega$$

where  $\boldsymbol{\alpha}_v = \mathbf{A} \tilde{\omega}' \tilde{\omega}'^T \mathbf{u}' - \mathbf{A} \tilde{\mathbf{u}}' \dot{\mathbf{G}}' \dot{\boldsymbol{\beta}}$  and  $\tilde{\omega}'$  is the skew symmetric matrix corresponding to the angular velocity vector  $\omega'$  of the rigid body in the local coordinate system. The “ $\bullet$ ” denotes the derivative with respect to time. The second term on the right-hand-side of Eq. (1) is the vector of generalized forces.

$$\mathbf{Q}_e = \begin{bmatrix} (\mathbf{Q}_e)_R \\ (\mathbf{Q}_e)_\beta \end{bmatrix} = \begin{bmatrix} \mathbf{F}_g + \mathbf{F}_c \\ \mathbf{G}^T \mathbf{M}_c \end{bmatrix}$$

where  $\mathbf{G} = \mathbf{A} \mathbf{G}'$ . The general force includes the gravitational force  $\mathbf{F}_g$  and the impact contact force  $\mathbf{F}_c$  and  $\mathbf{M}_c$  is the vector of the moment of contact force with respect to the mass center. The modeling of impact contact force will be given in Section 3.

The matrix  $\mathbf{M}$  is assumed to be positive definite, and Eq. (1) can be written as

$$\ddot{\mathbf{q}} = \mathbf{M}^{-1} [\mathbf{Q}_v + \mathbf{Q}_e]. \quad (2)$$

Introducing the state vector

$$\mathbf{U} = \begin{bmatrix} \dot{\mathbf{q}} \\ \mathbf{q} \end{bmatrix}$$

and the load vector

$$\mathbf{R} = \begin{bmatrix} \mathbf{M}^{-1} [\mathbf{Q}_v + \mathbf{Q}_e] \\ \dot{\mathbf{q}} \end{bmatrix},$$

Eq. (2) can be written as

$$\dot{\mathbf{U}} = \mathbf{R}. \quad (3)$$

Eq. (3) represents a set of ordinary differential equations, which can be solved for given initial conditions. The time integration is accomplished using the third order total-variation-diminishing (TVD) Runge–Kutta method, see Ref. [13].

### 3. Continuous contact model

As mentioned earlier, the purpose of the present work is to study the collision of a rigid body with the horizontal floor. The continuous contact model, also known as the compliant contact model [8,9], is used to model the impact contact force. This model is well suited for the problems under discussion. First, the model allows us to record specific impacts and forces at any particular moment; and two, the viscoelastic parameters in the model can be used to describe the energy dissipation and elastic reconstitution of the floor. As we are more concerned with the trajectory of the impacts rather than micro-collisions, we consider this continuous contact model adequate. Below we give a brief description of the numerical procedure; more detail will be given in an upcoming companion paper.

The horizontal ground is modeled as a distributed viscoelastic foundation, which consists of a layer of continuously distributed parallel springs and dampers, as shown in Fig. 2. Similar ground models have been used in [8,9] to study

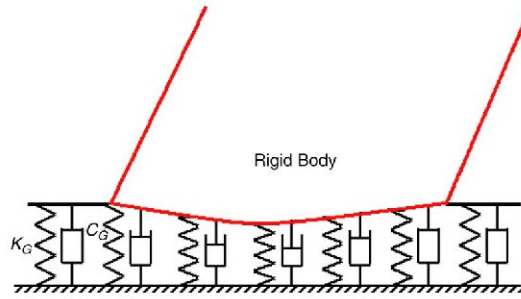


Fig. 2. Distributed viscoelastic foundation.

the impacts of concentrated masses or of rigid bodies with point impact contact. The surface stiffness is represented by the spring coefficient  $k_G$ , and  $c_G$  is the ground damping coefficient.

The impact contact force is calculated as the integration of a distributed load over the contact area  $s$  in the following form:

$$\mathbf{F}_c = \int_S \mathbf{f}_c dS \quad (4)$$

where  $\mathbf{f}_c = f_n \mathbf{n} + f_t \mathbf{t}$  is the vector of the distributed load.  $\mathbf{n}$  and  $\mathbf{t}$  represent the unit vector in the normal and tangential directions, respectively. The normal distributed contact load  $f_n$  is determined explicitly by the local indentation  $\delta$  and its rate of change.

$$f_n = (k_G + c_G \dot{\delta}) \delta.$$

The local tangential contact load  $f_t$  is computed using Coulomb's law. When sticking occurs, one has

$$f_t \leq \mu_s f_n \quad (5)$$

where  $\mu_s$  is the coefficient of static friction. When sliding occurs, one has

$$f_t = \mu_k f_n \quad (6)$$

where  $\mu_k$  is the coefficient of sliding friction.

The moment of impact contact force with respect to the mass center is computed as

$$\mathbf{M}_c = \int_S \mathbf{m}_c dS \quad (7)$$

where  $\mathbf{m}_c = \tilde{\mathbf{u}} \mathbf{f}_c$ , and  $\tilde{\mathbf{u}}$  is the skew symmetric matrix corresponding to the local position vector expressed in the global coordinate system.

In this computational model, the three-dimensional rigid body is described by a finite element type mesh that consists of a hexahedral, triangular-based prism, and tetrahedral elements. For impacts between rigid bodies with complex geometries, the impact contact surface is usually irregular. In this study, we assume the ground surface is flat. For the purpose of impact surface detection, the surface of the rigid body is partitioned by some triangular and quadrilateral surface elements. In the first stage of searching for a surface element that makes contact with the ground, any surface node that contacts with the ground is marked as the impact node, shown as solid dots in Figs. 3 and 4, where all possible cases are given for the triangular and quadrilateral surface elements. The surface element that contains at least one impact node is marked as the impact element. In the second stage of searching, each edge of the impact element is considered; for any edge with only one end node marked as the impact node, a new impact edge point, shown by empty circles in Figs. 3 and 4, may be added to that edge to mark the contact and non-contact parts of the edge. All the impact edge points and impact nodes in one surface element will be numbered and linked in proper order to form a closed polygon, as shown by the shaded areas in Figs. 3 and 4, which is considered as the approximation to the actual impact contact region in that element. For a triangular surface element, the impact contact

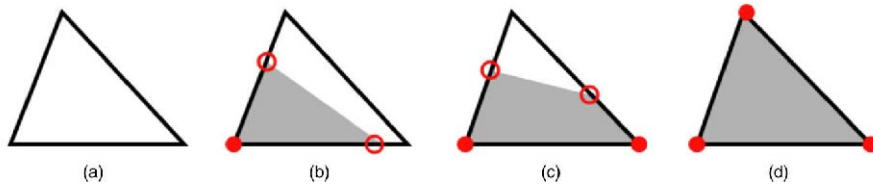


Fig. 3. Impact contact region for a triangular surface element.

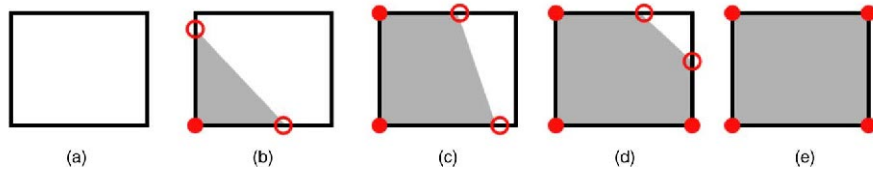


Fig. 4. Impact contact region for a quadrilateral surface element.

region could be a triangle or a quadrangle. For a quadrilateral surface element, the impact contact region could be in the shape of a triangle, quadrangle, or pentagon. After the contact regions are identified, the local contact load  $\mathbf{f}_c$  on each vertex of the contact region will be calculated based on its local indentation and relative velocity. The local impact moment load  $\mathbf{m}_c$  on each contact point with respect to the center of mass is also calculated. Finally total impact contact force and moment are calculated by Eqs. (4) and (7) using the standard Gaussian–Legendre quadrature.

When Coulomb's law is used to calculate the friction force during the impact, if the contact region of the rigid body is sliding on the ground surface during the impact, Eq. (6) will be used to calculate the tangential friction load. Assuming that sticking occurs during the impact, the unknown tangential force as part of the solution can be solved with a presumed sticking location. The resultant tangential force will be compared to its maximum value allowed by Coulomb's law; if it exceeds the maximum possible value, sticking will not happen and a recalculation will be conducted using Eq. (6) to compute the tangential friction load.

This continuous contact model is able to simulate three-dimensional impact dynamics, though most of the examples given in this paper are planar impact problems. The continuous contact model will be used to evaluate the impact contact force in the rigid body dynamics model of Section 2. The numerical simulation results of the falling rod problem will be given in Section 5.

#### 4. Discrete contact dynamics model for a falling rod

This section presents a discrete contact dynamics model for the falling rod problem. This model is based on the linear impulse-momentum principle, the angular impulse-momentum principle for the rigid body, and some impact parameters that relates the pre- and post-impact variables, such as the coefficient of restitution, which is defined as the ratio of the post-impact relative normal velocity to the pre-impact relative normal velocity at the impact location. The discrete model assumes that the impact occurs instantaneously and the impact forces are high, and thus the change in position and orientation of the rod during the contact duration are negligible and the effects of other forces (e.g. gravitational force) are disregarded [4]. This model is able to predict post-impact status for given pre-impact information and pre-defined impact parameters. The theoretical solutions in this section from the discrete model will be compared with the numerical results of the continuous impact model in Section 5.

The problem of a falling rod colliding with the horizontal ground is shown in Fig. 5. The length of the rod is  $L$ . The rod forms an initial contact angle  $\theta$  with the floor when one of its ends hits the ground. The unit vectors  $\mathbf{n}$  and  $\mathbf{t}$  define the normal and tangential directions. The vector pointing from the mass center of the rod to the impact location is defined as  $\mathbf{d} = d_n \mathbf{n} + d_t \mathbf{t}$ , and therefore

$$d_n = -\frac{1}{2}L \sin \theta, \quad d_t = -\frac{1}{2}L \cos \theta.$$

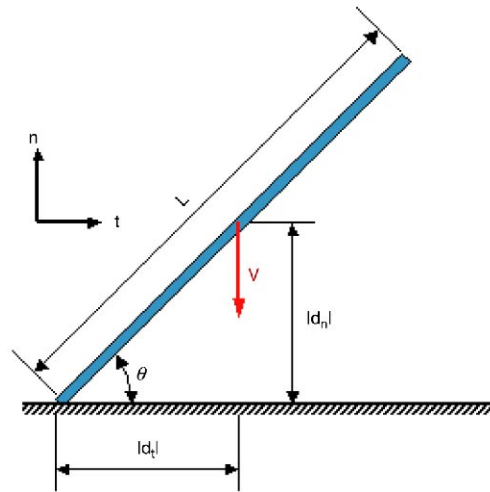


Fig. 5. Falling rod colliding with massive horizontal surface.

The impact dynamics equations consist of the following four equations:

$$\begin{cases} m(V_n - v_n) = P_n \\ m(V_t - v_t) = \mu_i P_n \\ \frac{1}{12}mL^2(\Omega - \omega) = \mu_i P_n d_n - P_n d_t \\ V_n - \Omega d_t = -e(v_n - \omega d_t). \end{cases} \quad (8)$$

The first two equations in (8) represent the linear impulse-momentum law in the normal and tangential directions. The third equation derives from the angular impulse-momentum law. The last equation gives the relation between the relative normal velocity at impact location before and after impact. The mass of the rod is given by  $m$ . The pre- and post-impact vectors of velocity at the center of mass of the rod are defined as  $\mathbf{v} = v_n \mathbf{n} + v_t \mathbf{t}$  and  $\mathbf{V} = V_n \mathbf{n} + V_t \mathbf{t}$ , respectively. The variables  $\omega$  and  $\Omega$  are the pre- and post-impact angular velocities of the rod. The impact impulse vector is given by  $\mathbf{P} = P_n \mathbf{n} + P_t \mathbf{t}$ , with its normal component  $P_n$  and tangential component  $P_t$ . The relation between these two components is given by  $P_t = \mu_i P_n$ , where  $\mu_i$  is the impulse ratio. The restitution coefficient is denoted by  $e$ . When the pre-impact variables and the impact parameters ( $\mu_i$  and  $e$ ) are known, Eq. (8) represents a closed system of algebraic equations for the following four unknowns:  $V_n$ ,  $V_t$ ,  $\Omega$ , and  $P_n$ . Setting  $m = 1$ ,  $L = 1$ ,  $\omega = 0$ , and  $e = 1$ , the solutions to Eq. (8) are given by

$$\begin{aligned} V_n &= -\frac{1 - 3 \cos^2 \theta + 3 \mu_i \sin \theta \cos \theta}{1 + 3 \cos^2 \theta - 3 \mu_i \sin \theta \cos \theta} v_n \\ V_t &= v_t - \frac{2 \mu_i}{1 + 3 \cos^2 \theta - 3 \mu_i \sin \theta \cos \theta} v_n \\ \Omega &= \frac{12 (\cos \theta - \mu_i \sin \theta)}{1 + 3 \cos^2 \theta - 3 \mu_i \sin \theta \cos \theta} v_n \\ P_n &= -\frac{2 v_n}{1 + 3 \cos^2 \theta - 3 \mu_i \sin \theta \cos \theta}. \end{aligned} \quad (9)$$

Note that the third equation in (8) is based on the assumption of point contact, and becomes invalid when  $\theta = 0$ . In this case, Eq. (8) reduces to the following set of equations:

$$\begin{cases} m(V_n - v_n) = P_n \\ m(V_t - v_t) = \mu_i P_n \\ V_n = -e v_n. \end{cases} \quad (10)$$

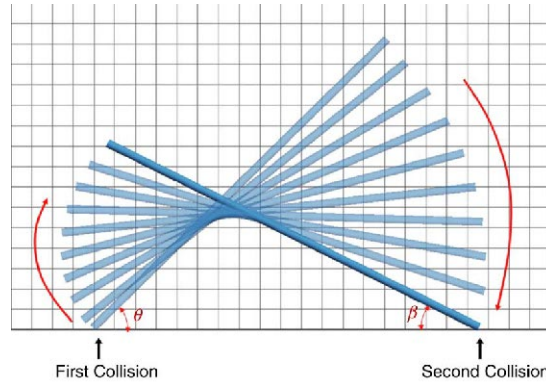


Fig. 6. The positions of the rigid rod at different times between the first and the second impacts.

When  $e = 1$ , we get solutions to Eq. (10):

$$\begin{cases} V_n = -v_n \\ V_t = -2\mu_i v_n + v_t \\ P_n = -2v_n. \end{cases} \quad (11)$$

Note that in Eqs. (8) and (10) the gravitational force is ignored. From now on in this section, we neglect the effect of friction ( $\mu_i = 0$ ) as well for simplicity. After the first impact, the velocities at two ends (denoted by subscripts  $a$  and  $b$ ) of the rod are

$$\begin{aligned} \mathbf{V}_a &= \mathbf{V}_1 + \boldsymbol{\Omega}_1 \times \mathbf{R}_a = \left\{ \frac{6 \cos \theta \sin \theta}{1 + 3 \cos^2 \theta}, -1 \right\}^T v_n \\ \mathbf{V}_b &= \mathbf{V}_1 + \boldsymbol{\Omega}_1 \times \mathbf{R}_b = \left\{ -\frac{6 \cos \theta \sin \theta}{1 + 3 \cos^2 \theta}, -\frac{1 - 9 \cos^2 \theta}{1 + 3 \cos^2 \theta} \right\}^T v_n. \end{aligned}$$

The subscript 1 stands for the first impact.  $\mathbf{V}_1$  is the velocity vector at mass center after the first impact.  $\boldsymbol{\Omega}_1$  is the vector of post-impact angular velocity for the first impact.  $\mathbf{R}_a$  and  $\mathbf{R}_b$  are vectors pointing from mass center to the two ends of the rod. When  $\theta \rightarrow 0$ , this is consistent with [1].

The solutions in (9) and (11) give the value of the post-impact variables after the first impact. If we assume that the time interval between the first and the second impact is very small and the gravitational force is neglected, the displacement and rotation of the rod is easily tracked, as shown in Fig. 6.

For the second impact, we designate the contact angle to be  $\beta$ . Without the small angle assumption, the relationship of inclination angle at each impact becomes complicated. Let the height of mass center of the rod at the first impact to be  $h$ , and the time duration of airborne to be  $T$ , the following relations hold if we ignore the effect of gravity,

$$\begin{cases} h = (\sin \theta)/2 \\ h + V_{1n} T = (\sin \beta)/2 \\ \beta + \theta = \Omega_1 T. \end{cases}$$

This leads to the following equation that relates the contact angles of the first and the second impact:

$$\sin \theta + \frac{1 - 3 \cos^2 \theta}{6 \cos \theta} (\theta + \beta) = \sin \beta. \quad (12)$$

There are two special angles where the relationship can be easily verified: (1) when  $\theta \rightarrow 0$ ,  $\theta = 2\beta$ ; (2) when,  $\theta = \arccos \frac{1}{\sqrt{3}}$ ,  $\theta = \beta$ . For a given first impact contact angle  $\theta$ , Eq. (12) can be solved for contact angle  $\beta$  of the second impact using *Mathematica* software [14]. The results are shown in Fig. 7, which indicates that  $\beta$  increases as  $\theta$  increases. This result can be used to classify different cases for the first two impacts of a clattering sequence, as illustrated by Fig. 8. When  $\theta < 58^\circ$ , the second impact occurs because  $\beta < 90^\circ$ , as shown by Fig. 8(a). We note here that the contact angle  $\beta \rightarrow 90^\circ$  when  $\theta \rightarrow 58^\circ$ . This corresponds to the marginal situation shown in Fig. 8(b),

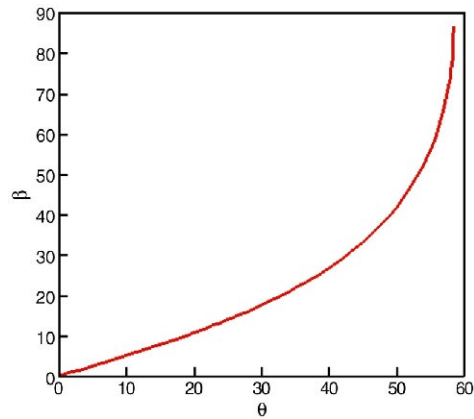


Fig. 7. The contact angle at second impact as a function of the initial contact angle.

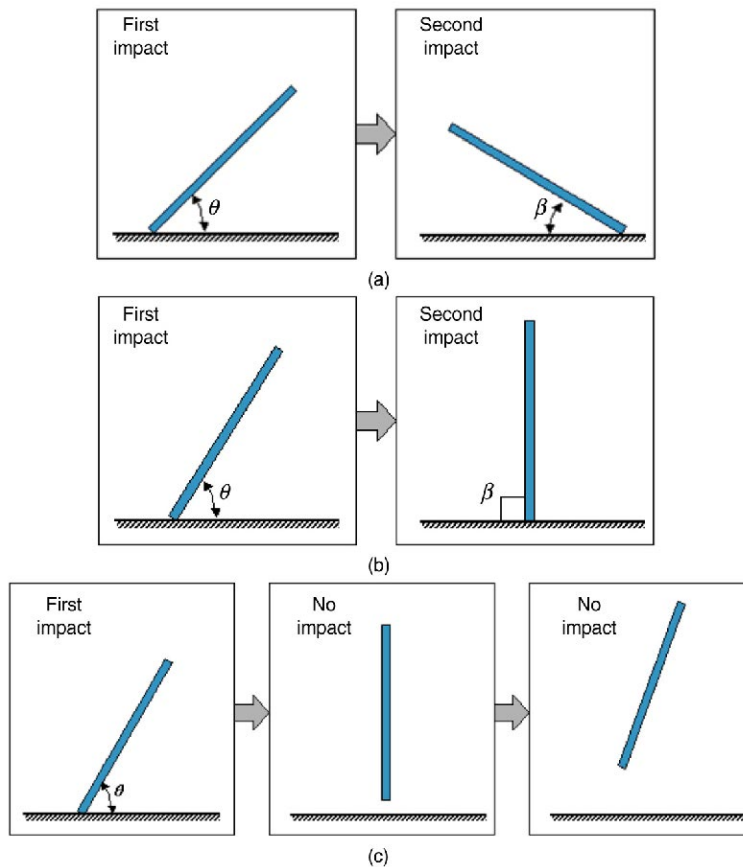


Fig. 8. From top to bottom, the diagram shows the transition from two-impact clattering to one impact. (a) When the dropping angle is smaller than the critical angle of about  $58^\circ$ , clattering involves two impacts: one at the left end and then one at the right end. After the first impact, the velocity at center of mass is positive (pointing upward), and rotation is clockwise. After the second impact, the velocity at center of mass is positive, and rotation is anticlockwise. (b) At the critical angle of about  $58^\circ$ , the second impact occurs when the rod is in a vertical position. (c) When the dropping angle is greater than the critical angle of about  $58^\circ$ , clattering becomes a single impact at the left end and there is no following impact. After the first impact, the velocity at center of mass is positive, and rotation is clockwise.

where the rod is in its vertical position when the second impact occurs. For the case of  $\theta > 58^\circ$ , because the gravity is ignored, there is no second impact, as the rod takes off after the first impact, see Fig. 8(c).



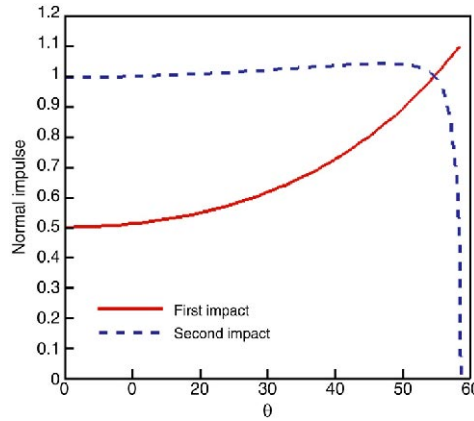


Fig. 9. Comparison of the normal impulse as a function of initial contact angle in the first and the second impact. At small angles the second impact is about twice that of the first one. They are equal at  $\theta = \arccos \frac{1}{\sqrt{3}}$ , and then the second angle quickly decreases to zero.

For the second impact, the variables can be obtained as follows.

$$\begin{aligned}
 v_{rn} &= \frac{1 - 3 \cos^2 \theta}{1 + 3 \cos^2 \theta} v_n - \cos \beta \frac{6 \cos \theta}{1 + 3 \cos^2 \theta} v_n \\
 V_{2n} &= -\frac{1 - 3 \cos^2 \theta}{1 + 3 \cos^2 \theta} v_n + \frac{2}{1 + 3 \cos^2 \beta} v_{rn} \\
 V_{2t} &= 0 \\
 \Omega_2 &= \frac{12 (\cos \theta)}{1 + 3 \cos^2 \theta} v_n + \frac{12 (\cos \beta)}{1 + 3 \cos^2 \beta} v_{rn} \\
 P_{2n} &= \frac{2}{1 + 3 \cos^2 \beta} v_{rn}
 \end{aligned}$$

where  $v_{rn}$  is the normal component of the relative velocity at the impact contact point. After the second impact, the velocities at both ends of the rod are

$$\begin{aligned}
 \mathbf{V}_a &= \mathbf{V}_2 + \boldsymbol{\Omega}_2 \times \mathbf{R}_a = \{0, V_{2n}\}^T + \boldsymbol{\Omega}_2 \{\sin \beta, \cos \beta\}^T v_n / 2 \\
 \mathbf{V}_b &= \mathbf{V}_2 + \boldsymbol{\Omega}_2 \times \mathbf{R}_b = \{0, V_{2n}\}^T - \boldsymbol{\Omega}_2 \{\sin \beta, \cos \beta\}^T v_n / 2
 \end{aligned}$$

where  $\mathbf{V}_2$  is the velocity vector at mass center after the second impact.  $\boldsymbol{\Omega}_2$  is the vector of post-impact angular velocity for the second impact.

We compare the normal impulse caused by the first and the second impact in Fig. 9. At the very small angle, the second impact is twice as large as the first one. Finally when the contact angle reaches a special value of  $\theta = \arccos \frac{1}{\sqrt{3}} \approx 54.74^\circ$ , the normal impulses are equal for the two impacts. As  $\theta$  further approaches  $58^\circ$ , the normal impulse of the second impact decreases sharply to zero, which agrees with the fact there is no clattering beyond that angle.

Now the contact angle  $\gamma$  of the third impact can also be calculated analytically. We illustrate in Fig. 10 the contact angle relation for all three impacts. It is noted here that for small  $\theta$ , a constant ratio of  $\theta:\beta:\gamma = 2:1:2$  holds for the contact angles. The sequence of the third impact ends around  $\theta = 27^\circ$  as there is no third impact when  $\theta > 27^\circ$ . In summary, the clattering sequence only involves two impacts when  $27^\circ < \theta < 58^\circ$ , and one impact when  $\theta > 58^\circ$ .

If gravity is included in the analysis, one extra term should be added to the left hand side of Eq. (12). Now the equation that relates the contact angles of the first and the second impacts becomes

$$\sin \theta + \frac{1 - 3 \cos^2 \theta}{6 \cos \theta} (\theta + \beta) + \frac{g}{2v_n^2} \left( \frac{1 + 3 \cos^2 \theta}{12 \cos \theta} \right)^2 (\theta + \beta)^2 = \sin \beta.$$

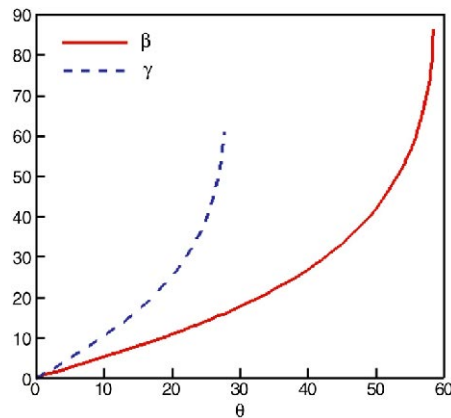


Fig. 10. The contact angle  $\gamma$  of the third impact is also a function of the initial contact angle  $\theta$ , and is imposed on the figure of second impact contact angle  $\beta$ .

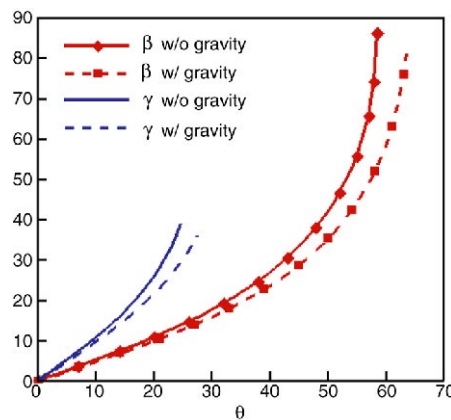


Fig. 11. The second impact contact angle  $\beta$  and the third impact contact angle  $\gamma$  as functions of the initial contact angle  $\theta$ , for the cases with or without gravity.

However, the inclusion of gravity in the equation does not change the fundamental properties of the clattering sequence under normal conditions of dropping, as indicated by Figs. 11 and 12. Fig. 11 compares the analytical solutions with and without gravity; the contact angles of the second and third impacts are plotted as functions of the initial contact angle of the first impact. The analytic solutions are quite similar for both cases with and without gravity. In Fig. 12, the normal impulse for the first, second, and third impacts are shown as functions of the initial contact angle for the cases with and without gravity. Again, qualitatively similar results are obtained for both cases. Compared to impact forces, the gravitational force is negligible during the impact. Thus the gravity only affects the motion between impacts. Since the time intervals between impacts are very small in a clattering sequence, inclusion of gravity only slightly changes the results of the second and third impacts. For simplicity, we ignore gravity in the analytic solutions given in this section. However, the numerical simulation based on the continuous contact model in Section 5 includes gravity, because the multiple impacts may not belong to the same clattering sequence and the time interval between impacts may be large,

## 5. Numerical simulation of falling rigid rod

The discrete contact dynamics model presented in the previous section is illustrative of qualitative features in clattering impact, but it certainly has several shortcomings. First of all, the discrete model is based on the assumption that the impact occurs instantaneously and the contact duration is negligible. Secondly, it also assumes that interaction forces are high, and thus the effects of other forces (e.g. gravitational force) are disregarded. Thirdly, it assumes the

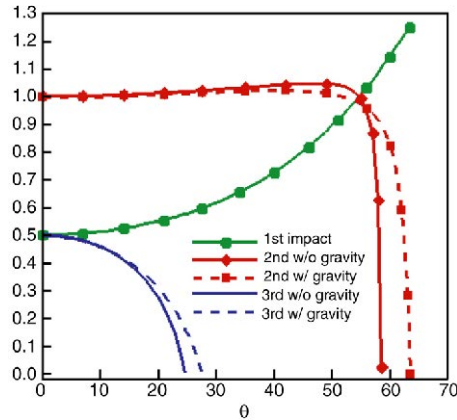


Fig. 12. The normal impulses of the first, the second, and the third impact as functions of the initial contact angle  $\theta$ , for the cases with or without gravity.

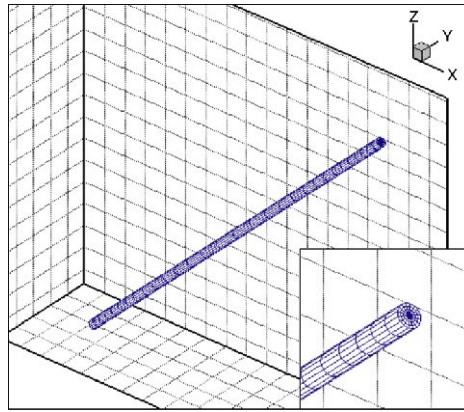


Fig. 13. Meshes at the surface of the falling rod.

impact is only with point-contact, and therefore the contact point must be known in advance. The discrete contact model needs to be modified to handle the case with multiple contact points or with surface-contact impact. The continuous contact model presented in Section 3 is able to overcome these problems. In this section, the rigid body dynamics equations given in Section 2 and the continuous contact model in Section 3 are applied to the numerical simulations of a falling rigid rod colliding with horizontal ground. The numerical results on the first impact are compared to analytic solutions of the discrete model for the purpose of code validation. Then the numerical results involving a sequence of multiple impacts of the falling rigid rod with the ground are displayed.

Fig. 13 shows the geometry and surface meshes of the rigid rod used in all test cases in this section. The rod is partitioned with 1920 three-dimensional elements, and there are 64 surface elements on each end of the rod and 480 surface elements on the side of the rod. The parameters of the rod are given as follows: mass  $m = 1$ , length  $L = 1$ , and radius  $r_d = 0.01$ .

In the first test case, the falling rigid rod collides with the horizontal ground at different contact angles  $\theta$  ranging from  $0^\circ$  to  $90^\circ$ . The initial angular velocity  $\omega = 0$ , pre-impact normal velocity  $v_n = -1$ , pre-impact tangential velocity  $v_t = 0$ , ground stiffness coefficient  $k_G = 10^{11}$ , and ground damping coefficient  $c_G = 0$ . The reason that  $k_G$  takes a large value is to make the contact surface small enough, such that the numerical results will be comparable to the analytic solution of the discrete contact model where a point-contact is assumed. The friction is not considered in this case, thus  $\mu_s = 0$  and  $\mu_k = 0$ . The discrete contact model in Section 4 is also used to find analytic solutions to this test case for comparison. In the discrete contact model, for the case of  $\theta \neq 0^\circ$ , the post-impact values are calculated by setting  $v_n = -1$ ,  $v_t = 0$ , and  $\mu_i = 0$  in Eq. (8). When  $\theta = 0^\circ$ , Eq. (10) is used to calculate the solutions. These solutions from the discrete contact model are referred to as the analytic solutions in this section.

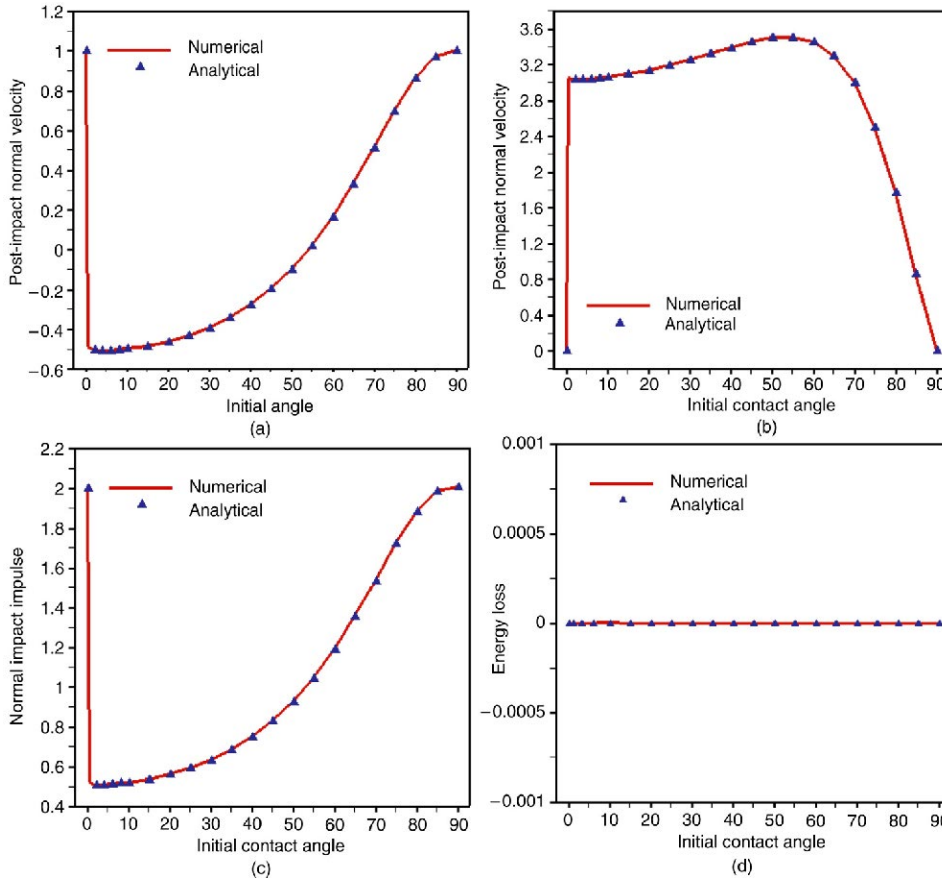


Fig. 14. Comparison between numerical and analytical results for the first impact of the rigid rod in the first test case. Mass  $m = 1$ , length  $L = 1$ , radius  $r_d = 0.01$ , initial angular velocity  $\omega = 0$ , pre-impact normal velocity  $v_n = -1$ , ground stiffness  $k_G = 10^{11}$ , ground damping coefficient  $c_G = 0$ , no friction. (a) Post-impact normal velocity of center of mass as a function of impact contact angle. (b) Post-impact angular velocity as a function of impact contact angle. (c) Normal impact impulse as a function of impact contact angle. (d) Energy loss as a function of impact contact angle.

The post-impact status of the rigid rod for the first impact given by numerical simulation is compared to the analytic solutions, as shown in Fig. 14. The post-impact normal ( $z$ -direction) velocity at mass center, the angular velocity, the normal impact impulse, and the energy loss are plotted as functions of the initial contact angles in Fig. 14(a)–(d). Both numerical simulation results and analytic solutions indicate a sudden change of velocity, angular velocity, and normal impact impulse when  $\theta$  changes from zero to non-zero values. In the numerical simulation, the normal impact impulse is computed as a time integration of normal impact force over the duration of impact:

$$P_n = \int_{t_1}^{t_2} F_n dt,$$

where  $F_n$  is the normal component of the impact contact force  $\mathbf{F}_c$ ,  $t_1$  and  $t_2$  are the instants corresponding to the beginning and the ending of the collision. The total energy of the rigid body is given as

$$E = T + P,$$

where  $T$  and  $P$  represent the kinetic energy and the potential energy, respectively. The kinetic energy can be calculated as

$$T = \frac{1}{2} m \dot{\mathbf{R}}^T \dot{\mathbf{R}} + \frac{1}{2} \omega^T \mathbf{I}_{\theta\theta} \omega,$$

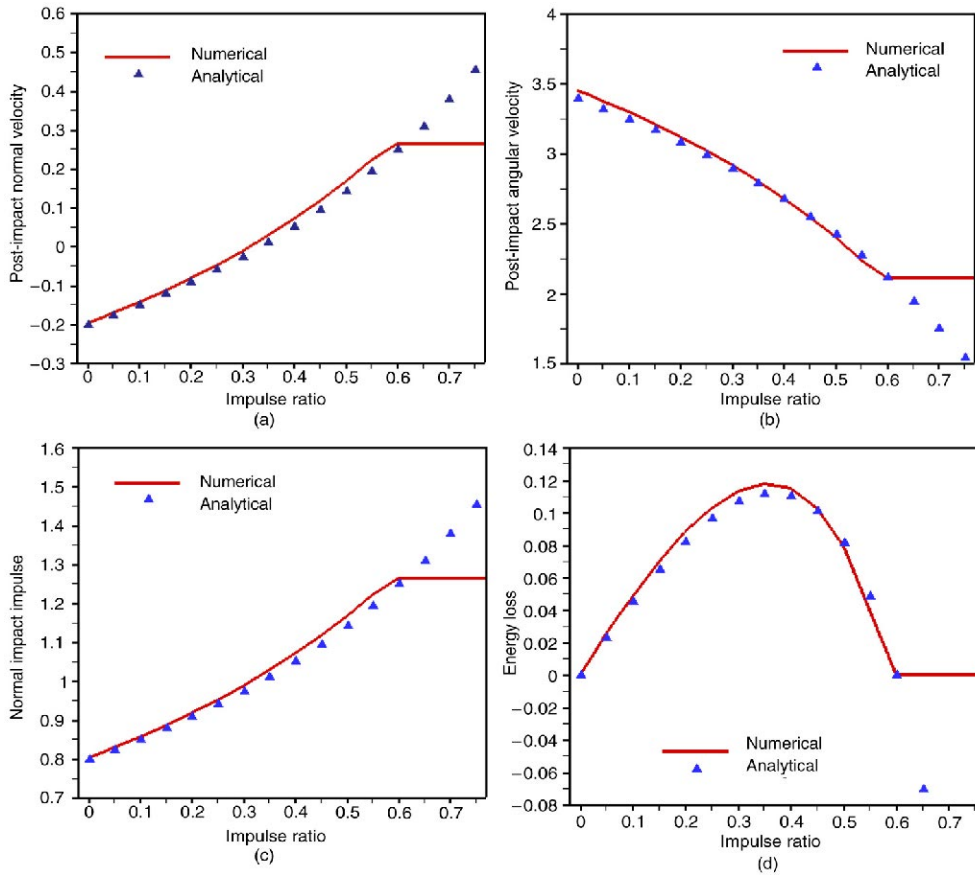


Fig. 15. Comparison between numerical and analytical results for the first impact of the rigid rod in the second test case. Mass  $m = 1$ , length  $L = 1$ , radius  $r_d = 0.01$ , initial impact contact  $\theta = 45^\circ$ , initial angular velocity  $\omega = 0$ , pre-impact normal velocity  $v_n = -1$ , ground stiffness  $k_G = 10^{11}$ , ground damping coefficient  $c_G = 0$ . (a) Post-impact normal velocity at center of mass as a function of impulse ratio. (b) Post-impact angular velocity as a function of impulse ratio. (c) Normal impact impulse as a function of impulse ratio. (d) Energy loss as a function of impulse ratio.

where  $\dot{\mathbf{R}}$  is the mass center velocity vector of the rigid body,  $\boldsymbol{\omega}$  is the vector of angular velocity, and  $\mathbf{I}_{\theta\theta}$  is the inertia tensor with respect to mass center. The first term on the right-hand-side of the above equation is the translational kinetic energy, and the second term is the rotational kinetic energy. The energy loss in the impact is the difference in total energy before and after the impact. Neither friction nor floor damping is included in this test case, the conservation of total energy is achieved by the simulation, as shown in Fig. 14(d). Overall, Fig. 14 indicates that the numerical results of rigid body dynamics simulation with continuous contact impact model agree very well with the analytic solutions.

The second test case demonstrates the collision of the falling rigid rod with the horizontal “rough” ground. The ground sliding friction coefficient  $\mu_k$  ranges from 0 to 0.8, representing different friction effects. The static friction coefficient  $\mu_s$  takes the same value as  $\mu_k$ . The initial impact contact angle  $\theta = 45^\circ$ . Other parameters are the same as in the first test case.

Setting  $\theta = 45^\circ$ , the analytic solutions in (9) give the post-impact value of different variables for the first impact. The comparisons between the analytic solutions and the numerical results are given in Fig. 15, where the impulse ratio  $\mu_i$  is calculated in the same way in both numerical results and analytic solutions. The post-impact values of normal velocity and tangential velocity at mass center are shown in Fig. 15(a) and (b) as a function of the impulse ratio. Fig. 15(c) shows the normal component of impact impulse for the first impact. The total energy loss in the first impact is shown in Fig. 15(d). When  $\mu_i < 0.6$ , the numerical results agree very well with the analytic solutions, but large deviations appear for  $\mu_i > 0.6$ . We note that the analytic solution based on the discrete contact model gives negative energy loss when  $\mu_i > 0.6$ , as shown in Fig. 15(d). Indeed, as pointed out by Brach [4], the impulse ratio  $\mu_i$

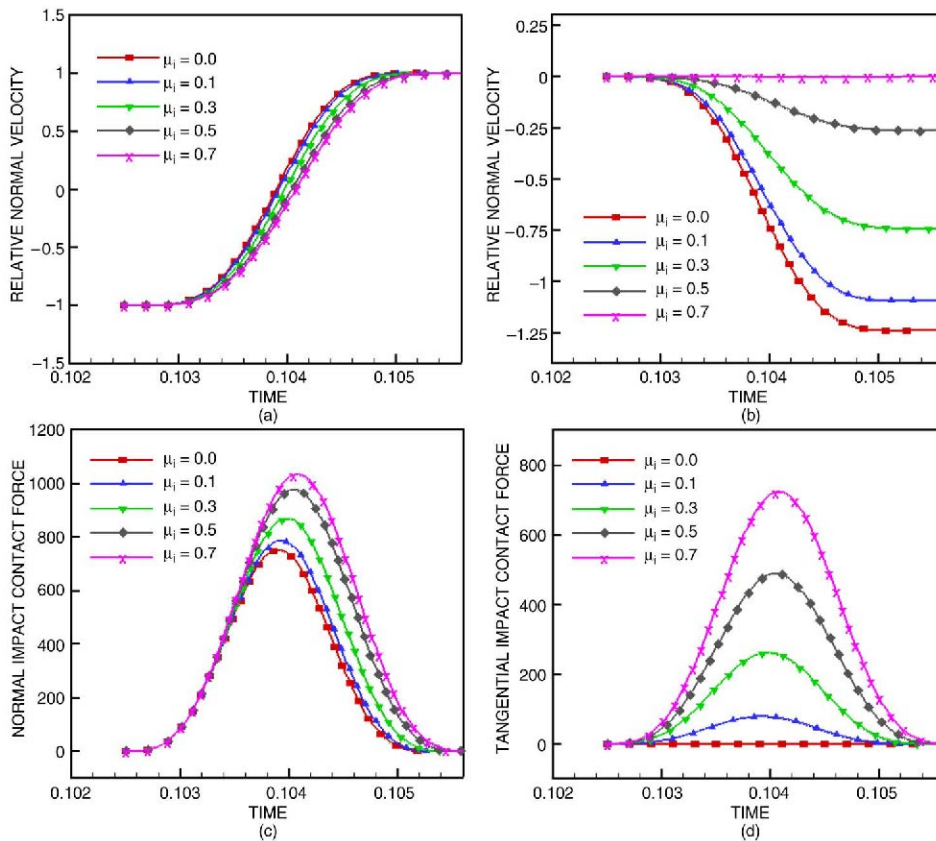


Fig. 16. Numerical results for the first impact of the rigid rod with the ground. All the parameters are the same as Fig. 15. (a) Relative normal velocity at the impact contact location as a function of time. (b) Relative tangential velocity at the impact contact location as a function of time. (c) Normal impact force as a function of time. (d) Tangential impact force as a function of time.

in the discrete contact dynamics model must satisfy  $|\mu_i| \leq \min(|\mu_O|, |\mu_T|)$  to ensure the conservation of energy. In our case,  $\mu_O = \mu_T = 0.6$  represents the upper limit of  $\mu_i$  to which the analytic solution of the discrete contact model is applicable. In Fig. 15, all curves of numerical solutions turn into horizontal lines when  $\mu_i > 0.6$ , indicating that the post-impact motion of the rod is independent of  $\mu_i$ . The explanation will be given later in this section. Compared to the failure of the discrete contact model, the numerical solutions of the continuous contact model give the correct answer.

One of the advantages of the continuous contact dynamics model over the discrete model is that it reveals the impact contact process explicitly and therefore is able to give details regarding the time-varying variables during the impact process. From the numerical simulation results of this test case, the variations of different quantities as functions of time during the first impact are presented in Fig. 16. Fig. 16(a) shows the normal component of the rod velocity at impact contact location. Each curve is corresponding to the result with a different impulse ratio. The normal velocity equals  $-1$  as the impact starts. During the impact process, the normal velocity at contact point gradually increases and reaches  $1$  at the end of the collision. When the ground damping coefficient  $c_G = 0$ , the numerical results are corresponding to the analytic solutions with the restitution coefficient  $e = 1$ . Fig. 16(b) shows the variation of the relative tangential velocity at contact location during the first impact at different impulse ratio  $\mu_i$ . Initially the tangential velocity is zero, and it becomes non-zero for all listed impulse ratios except  $\mu_i = 0.7$ , indicating that sliding occurs during the impact. When  $\mu_i = 0.7$ , the zero relative tangential velocity indicates sticking throughout the impact process. This is also reflected by the numerical simulation results shown in Fig. 15. As a matter of fact, in this test case, sliding occurs during the impact if the impulse ratio  $\mu_i < 0.6$ . When  $\mu_i > 0.6$ , the friction force becomes large enough to prevent the rod from sliding along the ground surface, therefore the relative tangential velocity at contact location becomes zero as the end of rod is sticking to the ground during the impact process. Once sticking occurs, the



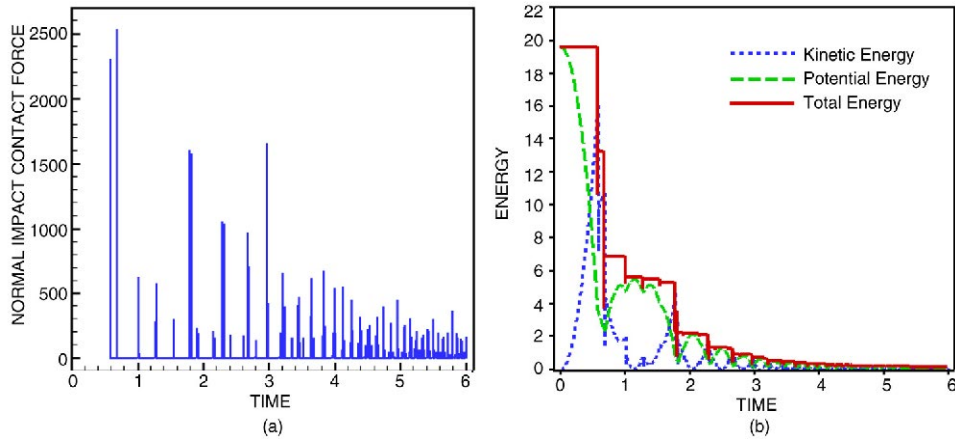


Fig. 17. Numerical results for multiple impacts of the rigid rod with the ground. Mass  $m = 1$ , length  $L = 1$ , radius  $r_d = 0.01$ , initial contact angle  $\theta = 45^\circ$ , initial angular velocity  $\omega = 0$ , initial elevation of center of mass  $z_c|_{t=0} = 2$ , ground stiffness  $k_G = 10^9$ , ground damping coefficient  $c_G = 10^8$ , static friction coefficient  $\mu_s = 0.35$ , and sliding friction coefficient  $\mu_k = 0.3$ . (a) Normal impact contact force as a function of time. (b) Total energy, kinetic energy, and potential energy as a function of time.

post-impact motion of the rod is independent of  $\mu_i$ , which explains why all the curves turn into horizontal lines when  $\mu_i > 0.6$  in Fig. 15. Fig. 15(d) also shows zero in energy loss when  $\mu_i > 0.6$ . This is because the damping effect of the ground is not included in this test case and no work is done by the friction force when sticking occurs. Fig. 16(c) and (d) display the variation of the normal and tangential impact contact force, indicating that larger friction induces a larger impact contact force along both normal and tangential directions.

The numerical simulation code developed in this study is able to study multiple impacts of the rigid body. The third test case is designed to demonstrate the numerical simulation of a sequence of impacts of the falling rod with the horizontal ground. The initial contact angle  $\theta = 45^\circ$ , initial angular velocity  $\omega = 0$ , pre-impact normal velocity  $v_n = -1$ , pre-impact tangential velocity  $v_t = 0$ , ground stiffness  $k_G = 10^9$ , and damping coefficient of the ground  $c_G = 10^8$ . The static friction coefficient  $\mu_s = 0.35$ , and the sliding friction coefficient  $\mu_k = 0.3$ . The numerical simulation results are summarized in Fig. 17. Fig. 17(a) shows the normal impact force as a function of time. Each spike is corresponding to one impact (some of the spikes are too close to each other in time and cannot be distinguished on the figure). Similar to the analytic solutions in Section 4, the second impact is larger than the first one. The third impact, apparently separated from the first two impacts by a larger time interval, does not belong to the same clattering sequence. The change of energy in the multiple impacts is given in Fig. 17(b). The horizontal line segments on the total energy curve indicate the conservation of total energy during the airborne time between the impacts. The energy loss that occurs during impact is attributed to ground damping and friction effect.

## 6. Numerical simulation of a simplified cell phone

In this section, we provide numerical simulation data for several scenarios of a cell phone falling from 1 m height at zero initial velocity and without initial rotation. The dimension and weight are obtained from public information to be same as a specific model of cell phone. The dimensions are 105.66 mm  $\times$  43.94 mm  $\times$  19.05 mm and weight is 88.14 g, as shown in Fig. 18. We limited our simulation to those cases relevant to clattering; a general simulation study is outside the scope of this article. The simulation results are shown as follows.

In the first simulation, the cell phone is uniformly inclined at  $10^\circ$  to the ground when it is released. No ground damping and friction effect is considered in this case. Fig. 19(a) and (b) show the variation of normal impact force and energy as functions of time for multiple impacts. In Fig. 19(a), the first two impacts, being very close in time, can be distinguished in the zoom-in window. The first clattering sequence is similar to the falling rod case where the peak normal impact force of the second impact is twice as large as that of the first impact. Since there is no ground damping and friction, the energy exchange between its kinetic part and potential part, with the conservation of total energy, is shown in Fig. 19(b). During the simulation, each collision is detected and the impact data are recorded. Fig. 20 shows the peak normal impact force for each impact and the elapsed time for each impact.

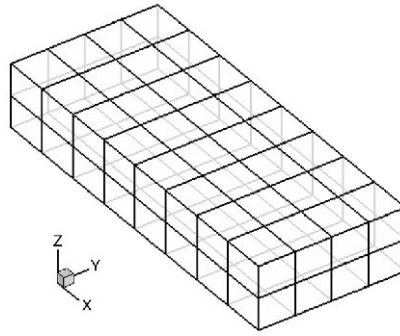


Fig. 18. Simplified cell phone model.

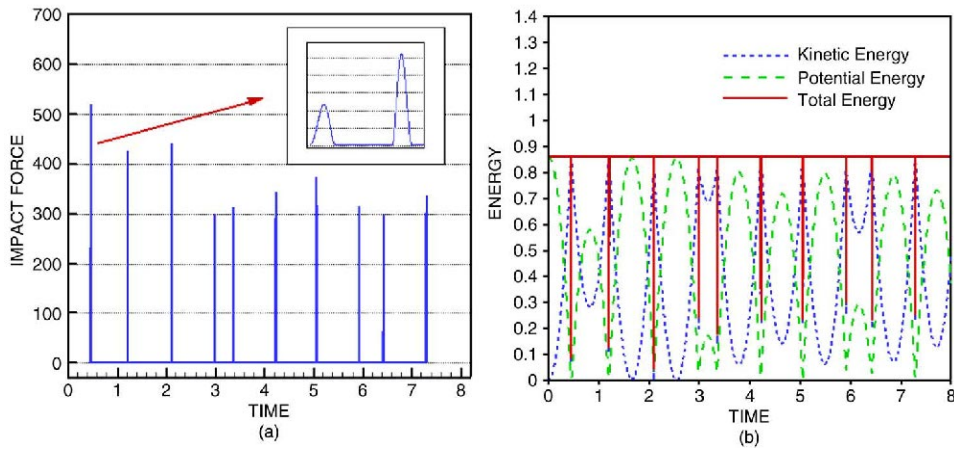


Fig. 19. Numerical results for multiple impacts of the model cell phone with the ground. Initial dropping angle  $\theta = 10^\circ$ , initial angular velocity  $\omega = 0$ , initial elevation of center of mass  $z_c|_{t=0} = 1$ , ground stiffness  $k_G = 10^8$ , ground damping coefficient  $c_G = 0$ , static friction coefficient  $\mu_s = 0$ , and sliding friction coefficient  $\mu_k = 0$ . (a) Normal impact contact force as a function of time. (b) Total energy, kinetic energy, and potential energy as a function of time.

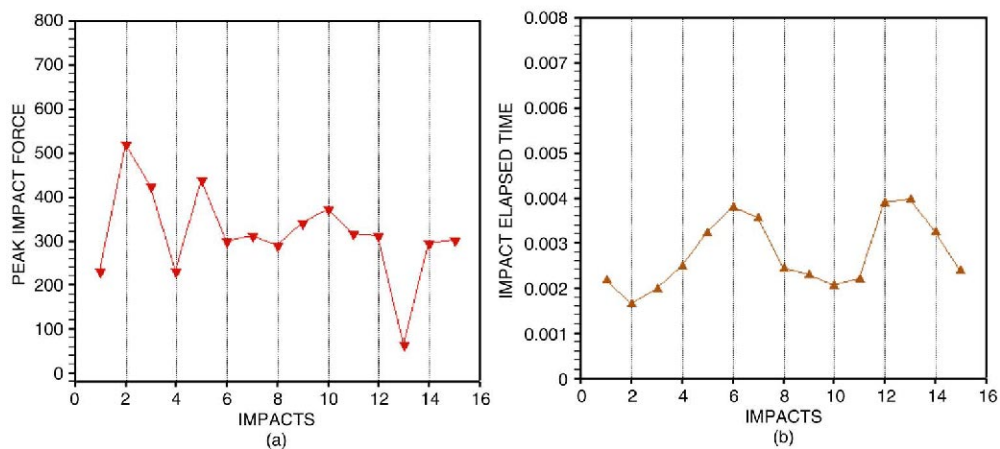


Fig. 20. Impact data for multiple impacts of the model cell phone with the ground. All the parameters are the same as Fig. 19. (a) Impact force for each impact. (b) The elapsed time for each impact.

In the second simulation of the falling cell phone, the setup is similar to the first simulation, except the ground damping and friction effect are included. The ground damping coefficient  $c_G = 10^7$ , the static friction coefficient



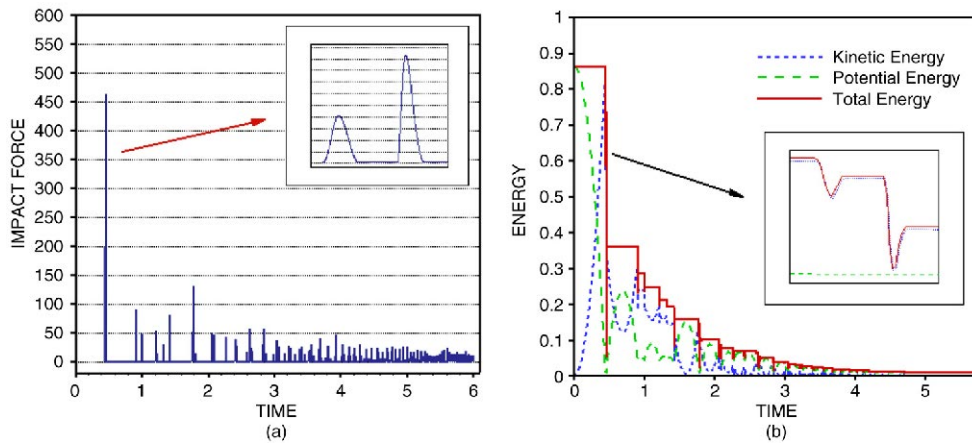


Fig. 21. Numerical results for multiple impacts of the model cell phone with the ground. Initial dropping angle  $\theta = 10^\circ$ , initial angular velocity  $\omega = 0$ , initial elevation of center of mass  $z_C|_{t=0} = 1$ , ground stiffness  $k_G = 10^8$ , ground damping coefficient  $c_G = 10^7$ , static friction coefficient  $\mu_s = 0.075$ , and sliding friction coefficient  $\mu_k = 0.075$ . (a) Normal impact contact force as a function of time. (b) Total energy, kinetic energy, and potential energy as a function of time.

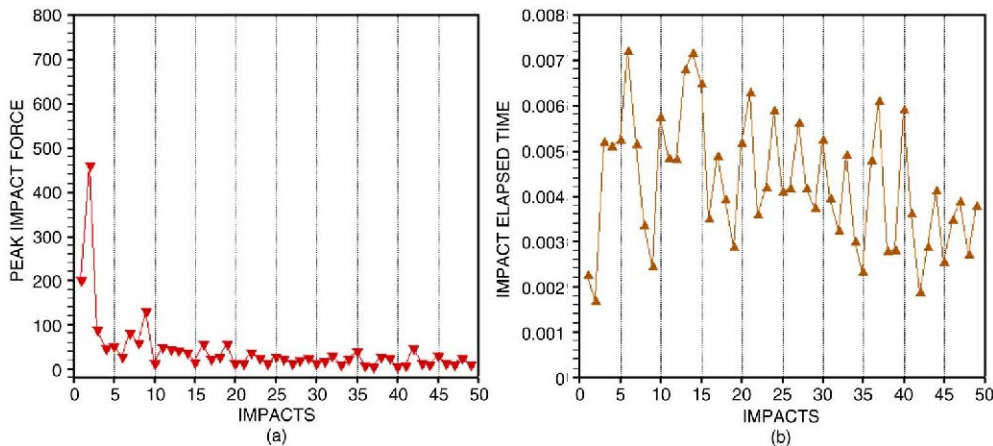


Fig. 22. Impact data for multiple impacts of the model cell phone with the ground. All the parameters are the same as Fig. 21. (a) Impact force for each impact. (b) The elapsed time for each impact.

$\mu_s = 0.075$ , and the sliding friction coefficient  $\mu_k = 0.075$ , all other parameters take the same value as in the first simulation. The variations of normal impact force and energy as functions of time during the multiple-impact process are displayed in Fig. 21(a) and (b). The first two impacts are nearly the same as in Fig. 19, except the peak impact force is slightly smaller. However, the cell phone has lost almost 60% of its total initial energy due to the damping and friction effect in the second impact, see the zoom-in window in Fig. 21(b). The peak impact force of the third impact and so on is much smaller than those in the first simulation. The impact data for each impact are shown in Fig. 22. Compared to the first simulation, the elapsed time for the subsequent impacts is substantially long in the second simulation.

To reveal more details about the energy loss during the first two impacts in this simulation, the zoom-in window in Fig. 21(b) is reproduced and shown in Fig. 23, where the translational and rotational kinetic energy are plotted separately. It seems that the transfer of kinetic energy between its rotational part and translational part is important to energy loss in the clattering process. For instance in Fig. 23, the first impact causes the transfer of a large portion of translational energy to rotational energy, so the rotational energy sharply increases during the first impact, and the cell phone rotates very fast after the first impact. In the second impact, which follows the first impact only by 0.004 s, a large portion of kinetic energy transfers from its rotational part to the translational part, and the peak normal impact

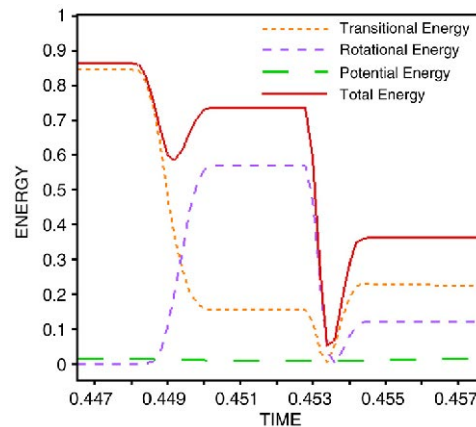


Fig. 23. Variation of energy for the first two impacts in the second simulation.

force produced by the second impact is twice as large as that in the first impact, see Fig. 22(a). The loss of total energy in the second impact is substantially greater than that in the first impact. Because the time interval between the first and the second impact is so small, the potential energy is almost a constant, as indicated by Fig. 23. Therefore, the gravity effect is trivial in this clattering sequence.

Finally, we conducted a series of numerical simulations for the first impact of the cell phone at different impact contact angles ranging from  $2^\circ$  to  $85^\circ$ . All the other parameters are the same as in the second simulation. In Fig. 24, the post-impact normal velocity at mass center, the post-impact angular velocity, the peak normal impact force, and the energy loss are plotted as functions of the impact contact angle. We find in Fig. 24 some similarity with Fig. 14, although two are in different geometric shapes and different initial velocities.

## 7. Discussion and conclusion

The overall aim of this article is to analyze both analytically and through numerical simulation the issues regarding clattering in multiple impacts of a rigid body. Our discussions are limited to a rod and a rectangular model cell phone with uniformly distributed mass. Our three-dimensional computational dynamics model however allows us to study the multiple-impact sequence of a rigid body with any shape and arbitrary distribution of mass. For the falling rod case, the numerical simulation based on the continuous contact model predicts the sliding and sticking that occur at the contact location correctly, while the analytic solution based on the discrete contact model fails when sticking occurs.

Our study confirms the results of Goyal et al. [1,2] that if a rod falls to the ground at a small angle, then its clattering impact series has a much larger second impact than the initial one. Furthermore, our analytic study finds that the same phenomenon is happening at angles as large as  $54^\circ$ . In realistic situations, the range might be small when the energy dissipation and friction effect of the ground are included in consideration, as our three-dimensional numerical model study shows. Clattering is also common in the falling of a three-dimensional object such as a cell phone, notebook computers and other mobile devices. The dynamics can be more complicated; the second impact can be more than twice that of the initial impact, as our numerical study shows.

It remains an interesting topic what is the true implication of clattering. On the one hand, it means the second impact cannot be ignored in analysis. On the other hand, our calculation shows that when the dropping inclination angle is small, the summation of the first three impacts equals the first impact at zero angle of drop. It seems to suggest clattering spreads the impact. Of course, in application to electronic devices, one needs to determine the effect of impact on the internal contents. A flexible body model incorporating the detailed structure of devices is helpful to test the effect of micro-collision, vibrations and shock wave propagation in the devices.

We find in our numerical study that the kinetic energy transfers between its rotational part and translational part are important for impact forces in a clattering sequence. Larger impacts typically occur at the transition from fast rotation to fast translation. Our numerical model has been proven to be a realistic tool for multiple-impact study.

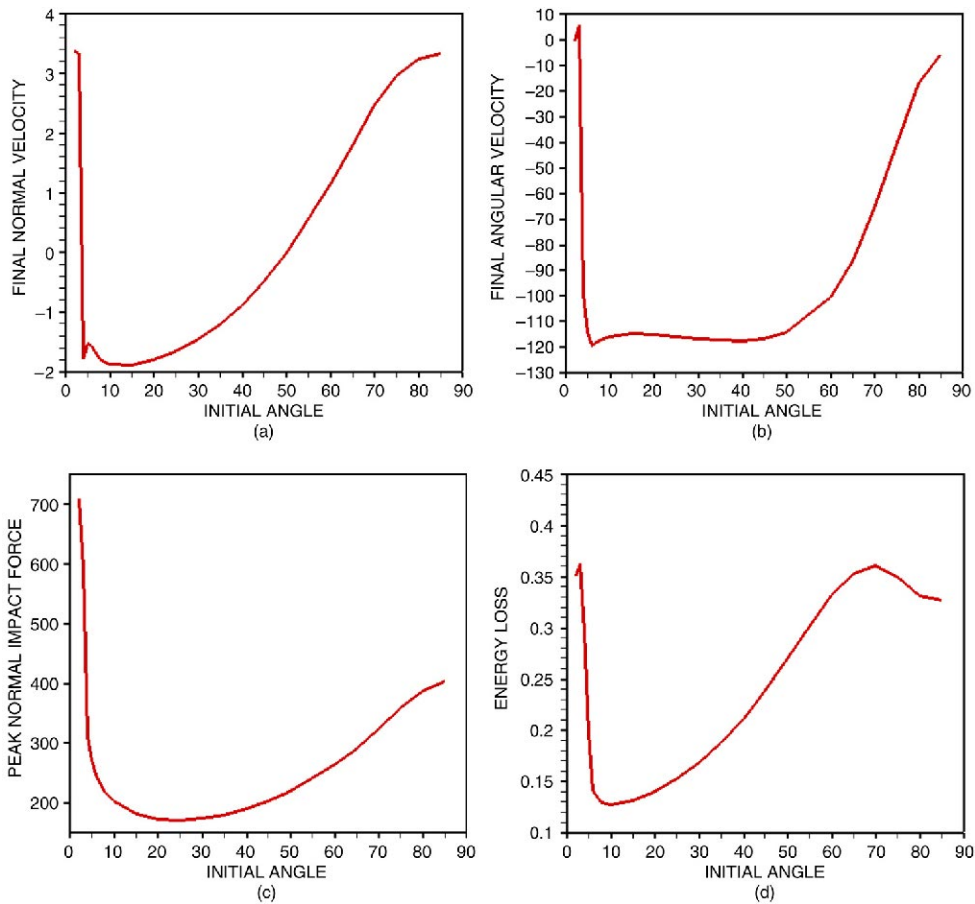


Fig. 24. Numerical results for the first impact of the model cell phone with ground. Initial dropping angle  $\theta = 2^\circ\text{--}80^\circ$ , initial angular velocity  $\omega = 0$ , initial elevation of center of mass  $z_c|_{t=0} = 1$ , ground stiffness  $k_G = 10^8$ , ground damping coefficient  $c_G = 10^7$ , static friction coefficient  $\mu_s = 0.075$ , and sliding friction coefficient  $\mu_k = 0.075$ . (a) Post-impact normal velocity at mass center as a function of impact contact angle. (b) Post-impact angular velocity as a function of impact contact angle. (c) Peak normal impact force as a function of impact contact angle. (d) Energy loss as a function of impact contact angle.

## Acknowledgement

This work is supported in part by Nokia University Fund.

## References

- [1] S. Goyal, J.M. Papadopoulos, P.A. Sullivan, The dynamics of clattering I: equation of motion and examples, *ASME J. Dyn. Syst. Meas. Control* 120 (1998) 83–93.
- [2] S. Goyal, J.M. Papadopoulos, P.A. Sullivan, The dynamics of clattering II: global results and shock protection, *ASME J. Dyn. Syst. Meas. Control* 120 (1998) 94–101.
- [3] J.B. Keller, Impact with friction, *ASME J. Appl. Mech.* 53 (1986) 1–4.
- [4] R.M. Brach, Rigid-body collision, *ASME J. Appl. Mech.* 56 (1989) 133–139.
- [5] W.J. Stronge, Rigid-body collision with friction, *Proc. R. Soc. London A* 431 (1990) 169–181.
- [6] D.E. Stewart, Rigid-body dynamics with friction and impact, *SIAM Rev.* 42 (2000) 3–39.
- [7] G. Gilardi, I. Sharf, Literature survey of contact dynamics modeling, *Mech. Mach. Theory* 37 (2002) 11213–11239.
- [8] D. Stoiyanovici, Y. Hurmuzlu, A critical study of the applicability of Rigid-body collision theory, *ASME J. Appl. Mech.* 63 (1996) 307–316.
- [9] A. Yigit, A. Ulsoy, R. Scott, Dynamics of radially rotating beam with impact, Part I: Theoretical and computational model, *J. Vib. Acoust.* 12 (1990) 65–70.
- [10] J. Wu, G. Song, C. Yeh, K. Waytt, Drop/Impact simulation and test validation of telecommunication products, in: *Intersociety Conference on Thermal Phenomena*, IEEE, 1998, pp. 330–336.

- [11] T. Tee, H. Ng, C. Lim, E. Pek, Z. Zhong, Application of drop test simulation in electronic packaging, in: ANSYS Conference, November 5–6, 2002.
- [12] A. Shabana, Computational Dynamics, 2nd edition, John Wiley & Sons, New York, 2000.
- [13] C.W. Shu, S. Osher, Efficient implementation of essentially non-oscillatory shock-capturing schemes, J. Comput. Phys. 75 (1988) 439–471.
- [14] S. Wolfram, The *MATHEMATICA* book, 4th edition, Cambridge University Press, Cambridge, UK, 1999.